DESIGN AND ANALYSIS OF DEPLOYMENT MECHANICS FOR A SELF-FOLDING, SPIRAL BASED SPACE-BORNE INTERFEROMETER

Kanak Parmar[*], **Manuel Indaco**[*], **Ryan Long**[*], **Will Taylor**[†], **Nathan Adkins**[‡], **Deepika Singla**[‡], **Russell W. Mailen**[§], and **Davide Guzzetti**[§]

Ground based observations of the 21-cm signal to study the cosmological Dark Ages are impeded both by the Earth's atmosphere, as well as man-made radio interference. Therefore, numerous concepts have proposed the use of space-based architectures to observe the 21-cm signal. Previously proposed architectures may be classified into monolithic spacecraft, lunar-based observatories, and satellite formations or swarms. Each architecture type may carry intrinsic shortcomings in cost, complexity, or achievable scientific return. To the series of space-based observatories for 21-cm signal detection, we add a novel concept that utilizes a kilometer-long strip of shape memory polymer (SMP) to actively deploy an orbiting, kilometer-sized, rigidly connected array of antennas in cislunar space. This SMP material will be marked by ink hinges that absorb solar infrared radiation to trigger a temperature gradient and induce folding of the SMP strip into a desired final geometry. If found feasible, this architecture can not only reduce mission complexity, but also decouple the final design from manufacturing and launch constraints, and offer more customizable geometries for interferometry. We currently target a final configuration of a 3 turn spiral with a diameter of 3 km. An appropriate deployment strategy to achieve this configuration is warranted. In this work, we initiated the SMP strip deployment analysis considering both kinematical relations and reduced fidelity dynamical behaviors based on modified double pendulum dynamics. These analyses concluded in the proposal of a sequential deployment strategy, where hinges are activated sequentially. We also consider induction of inertia loads to aid the folding process and reduce the dynamical impact of the increasing moment of inertia of the folded final configuration as deployment progresses.

INTRODUCTION

Observation of the cosmological 21-cm signal can greatly aid in the scientific understanding of the formation of the universe. Although most of the phases across the timeline of cosmological evolution have been experimentally observed, the Dark Ages period, which encompasses the era following the Big Bang but prior to the Epoch of Reionization, remains a scientific enigma. During this period, the temperature of the universe was low enough to allow light to travel for long distances,[1] but no sources active in the visible range, such as stars, existed. Furthermore, photons were produced by two main sources: the recombination/decoupling of neutral hydrogen atoms, and the occasional change of the energy state of hydrogen. The latter determines the 21-cm hydrogen

---

[*]Graduate Student, Department of Aerospace Engineering, Auburn University, 210 Davis Hall

[†]Undergraduate Student, Department of Mechanical Engineering, Auburn University, 1418 Wiggins Hall

[‡]Undergraduate Student, Department of Aerospace Engineering, Auburn University, 210 Davis Hall

[§]Assistant Professor, Department of Aerospace Engineering, Auburn University, 210 Davis Hall

line, the wavelength associated to the radiation emitted during energy state changes of the hydrogen atom. Due to redshift, this radiation reaches Earth today at frequencies about and below 30 MHz,[2] rendering ground based observations extremely challenging, if not impossible, due to both the Earth's ionosphere and anthropogenic radio emissions; consequently, alternative solutions for a Dark Ages radio observatory are warranted.

In general, observation of cosmological radio signals is accomplished via the use of ground-based interferometer arrays, which are collections of individual receiving antennas, operating in tandem, spread over a large distance. This results in higher spectral resolutions, and the exact geometry of antenna locations within the array can be designed to achieve desired angular measurement requirements. There have been various mission concepts that propose the use of space-based architectures as they would by-pass some of the limitations of ground-based antennas and potentially allow for the detection of the 21-cm signal at low and very-low radio frequencies. The trade space for a Dark Ages radio observatory can be roughly divided into three primary categories: lunar based architectures, satellite formations (< 10 individual elements), satellite swarms (10+ individual elements), and monolithic instruments, each with its own engineering trade offs in regards to cost, complexity and scientific return.

Lunar-based architectures, such as the Lunar Radio Array (LRA)[3] and FARSIDE,[4] rely on placing antennas at appropriately selected sites in order to observe cosmological signals. Although lunar-based architectures offer high scientific return as they may leverage Radio Frequency Interference (RFI) quiet zones, they are also characterized by high transportation costs and complex assembly operations on the lunar surface. Furthermore, power generation and Earth communications may potentially become critical design factors should the chosen antenna site be within a crater or close to the lunar polar regions. Finally, lunar-based architecture are highly sensitive to programmatic risk, as they depend on the separate implementation of lunar programs.

Satellite formations and swarm architectures, such as DARIS,[5] IRASSI,[6] SULFRO,[7] and OL-FAR,[8,9] allow for the utilization of interferometry techniques as each individual element of the architecture can be equipped with an antenna for signal measurement. As each element operates individually, as part of a larger whole, the architecture concept is highly robust and does not demonstrate a single point of failure. Although we list formations and swarms together, there are still some definitive differences between the architectures. Individual elements in formation architectures typically comprise of a regular sized spacecraft bus, and the total number may be limited by launch cost constraints. It should be noted that having a formation architecture of less than 10 elements may not be sufficient for measuring 21-cm spatial fluctuations. In contrast, swarm architectures allow for many more antennas, but may be limited by miniaturization, metrology and controllability challenges. It should be noted that the metrology and controllability of swarms is an area of low TRL, and the needed technology may not exist yet.

Monolithic architectures, such as the RAE-1[10] and DARE,[11] have high space legacy, but earlier missions did not provide high angular resolutions. Furthermore, architectures such as DARE are unable to perform tomographic measurements, as they are designed as a global signal instrument. In comparison, our proposed design exploits the benefits associated to these different architectures, while aiming to cope with their drawbacks: an orbiting, monolithic structure which accommodates a system capable of interferometric measurements; redundancy may be introduced so that single point of failure are avoided, while the large number of antennas prevents strong performance degradation in case of single antenna damage.
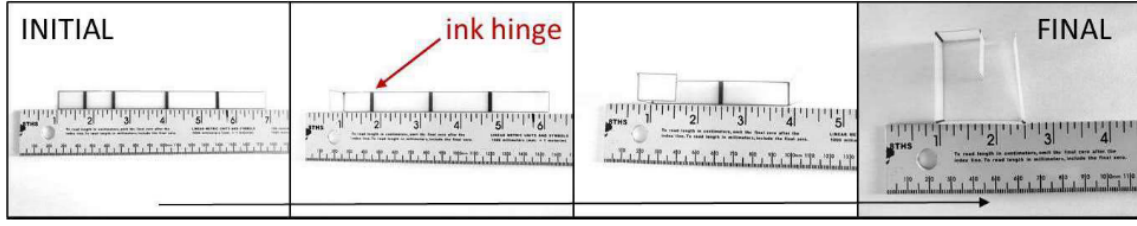
Figure 1: Example folding process for a lab SMP sample.

PROPOSED MISSION CONCEPT OF OPERATIONS

Different from previously proposed low-frequency radio observatories, we aim to study the feasibility of integrating an array of receivers on a multi-functional shape memory polymer (SMP) bus that is capable of self-folding when exposed to solar radiation. This technology may enable the flat fabrication of kilometer-sized antenna arrays for radio astronomy that self-transform into the operative configuration once in orbit. Because the receiving antennas are connected via the SMP bus, control and communications challenges that are typically of swarm solutions are mitigated. Because the resulting architecture is effectively a system of distributed sensors, 21-cm signal interferometry may be possible. Finally, because the system can be deployed in orbit environment, cost, complexity, and programmatic risk of lunar surface operations are by-passed.

Shape memory polymers are smart materials that can change shape in response to external stimuli, such as heat and infrared light absorption.[12, 13] SMP materials may be patterned with ink hinges that absorb infrared radiation and trigger a local temperature gradient. Once the glass transition temperature ($\sim 100°$) is reached, the local temperature gradient induces a folding behavior of the material. Ink hinge patterns may be designed to induce a change of the material shape into a desired final geometry; a visual example of the folding process is provided in Figure 1. This folding behavior can be controlled by the the darkness of the ink hinge, the intensity of the absorbed light energy, and the width of the ink hinge pattern. In addition, the possibility of printing, encapsulating or attaching electronics onto SMP sheets creates a powerful paradigm for fabrication and in-space assembly of a 21-cm line instrument.[14]

We envision creating an instrument for 21-cm signal detection at low and very-low frequency by placing a series of dipole antennas along a km-long SMP strip. The multi-functional, kilometer-long strip of SMP material may be manufactured on Earth, and subsequently wrapped into a co-planar spool that is able to fit within one of the currently available payload fairings. Once the observatories reaches the target destination, possibly the cislunar space, and is exposed to solar radiation, the self-deployment process begins. Ink hinges strategically placed along the SMP material will absorb incoming solar radiation, in the IR wavelength, and trigger a local temperature gradient that activates a self-folding behavior between adjacent ink-free regions, or facelets. By controlling the facelets' folding behavior, we can achieve a predefined final configuration for the interferometeric array that has a maximum baseline on the order of kilometers, allowing for greater angular resolutions of the measured signal. Once all facelets are folded into the desired configuration, on-orbit science observations will commence via use of the individually placed antennas. We currently propose the use of the cislunar region due to possibly lower mission costs as well the ability to leverage passage across RFI zones on the lunar farside along a specified orbit. The concept of operations (CONOPS) for this proposed design is illustrated in Figure 2.
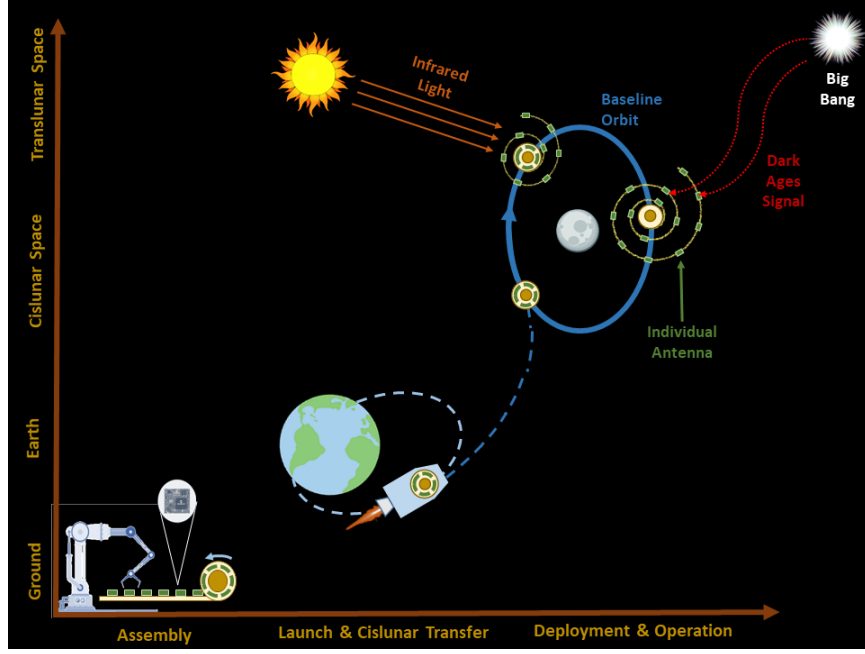
Figure 2: The concept of operations for the proposed architecture

SCIENTIFIC OBSERVATION OF THE 21-CM SIGNAL

The science observation capability of the deployed SMP is the primary driver in the design of this architecture. Therefore, understanding the relevant aspects of interferometric observation and radio astronomy is critical. Two modes of observation of the 21-cm signal are typically considered important to constrain cosmological models with observational evidence:[15] global-signal characterization (which produces an evolution of the sky-averaged 21-cm brightness in redshift) and tomography (which produces a map of spatial fluctuations of matter and hydrogen density at different redshift, thus enabling to represent the evolution of the early universe, as illustrated in Figure 3). The 21-cm signal is expected to be between 0 mK to 40 mK, with fluctuations in the order of 0.1-1 mK;[16] such intensity is about 10^5-10^6 orders of magnitude weaker than the foreground, consequently requiring noise removal techniques and long observation times.

In theory, a single dipole connected to a spectrometer would allow global signal detection; however, the addition of N dipoles leads to a reduction in the observation time of a factor $\sqrt{N}$.[17] Therefore, exploiting an interferometer may lead to some relevant advantages: firstly, using multiple antennas a faster detection of the global signal is possible; secondly, the interferometric nature of the architecture allows to reach higher levels of sensitivity and to lower the target frequency range with respect to monolithic architecture; finally, low resolution level for spatial fluctuations could be achieved.

Our proposed architecture currently comprises of 150, 5m-long, dipole antennas whose spacing is determined by the corresponding interferometer performance analysis, as further discussed in the next section. Our antenna architecture is currently designed to achieve a signal to noise ratio (SNR) of 5 with a sensitivity of about 1.5 mJy at 30 MHz, as computed via:

$$\Delta S = \frac{2kT_{sys}}{A_{eff,dipole}\sqrt{N(N-1)\Delta\nu\Delta t}} \tag{1}$$
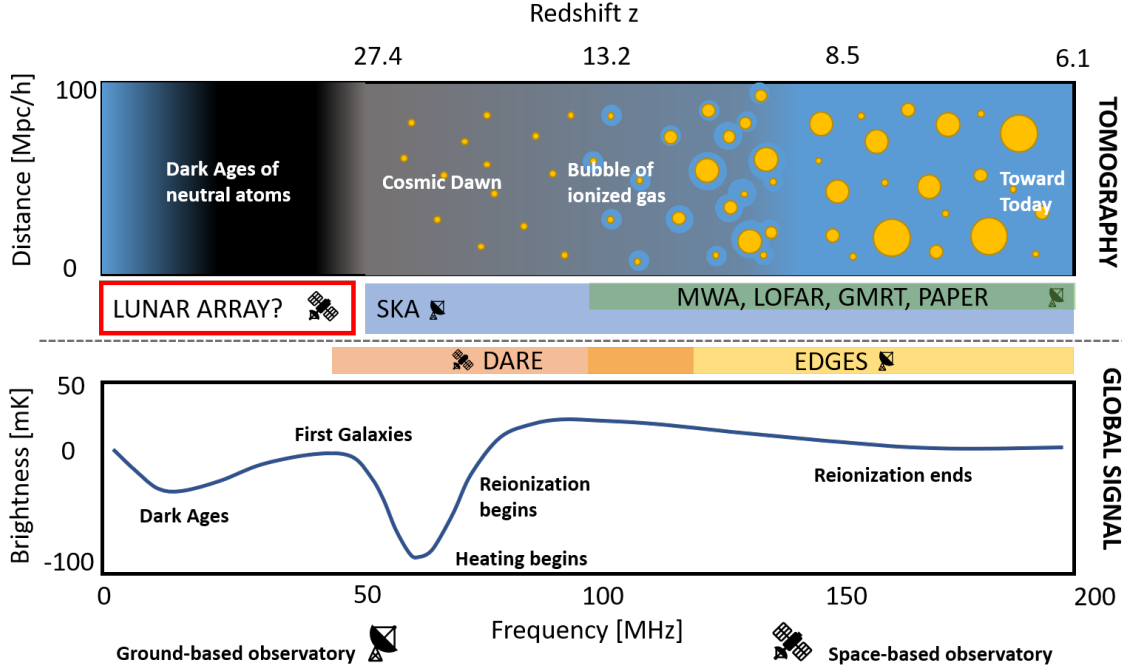
4

Figure 3: Current and planned observations and observatories for Tomography of the 21-cm signal (top panel) and sky-averaged global signal (bottom panel)

where the $N(N-1)$ is the number of baselines (i.e. combinatorial pairs of antennas in the array), $\Delta\nu$ is the instantaneous bandwidth (currently assumed to be 1 MHz), Δt is the observation time, k is the Boltzmann constant and T_{sys} is the system temperature, which is generally approximated through the sky temperature modeled as:[16]

$$T_{sky} = 16.3 \times 10^6 K \times \left(\frac{\nu}{2\ MHz}\right)^{-2.53} \tag{2}$$

Based on preliminary estimates, the required SNR at 30 MHz may be achieved in about 860 days of continuous observation.

UV PLANE INTERFEROMETER PERFORMANCE

As mentioned in the previous section, the observational capability of the deployed SMP array is determined by the design of the underlying antenna geometry embedded within the deployed architecture. The placement geometry of the antennas is known to impact the performance of the overall interferometer array,[18] and understanding these underlying relations will influence the final design geometry of the deployed SMP material, or SMP bus.

Compared to a traditional radio telescope, an interferometer array is not capable of directly producing an image of the source it is observing. Instead, it measures the Fourier Transform of the sky brightness distribution in a plane that is perpendicular to the plane of observation. A measurement along a given line between two observational antennas (which is also referred to as a baseline), corresponds to a particular point on the perpendicular plane and is denoted with coordinate variables *u* and *v* (the use of the variables *u* and *v* is for notation purposes and can be seen as analogous to Cartesian *x* and *y* coordinates). This perpendicular plane is also commonly referred to as the *uv*,

or aperture synthesis, plane and must be appropriately populated to achieve high-quality aperture synthesis mapping of a given source.

Provided a geometry consisting of individually placed antennas spanning a certain area, the *uv* points can be calculated by finding the distance between each combinatorial pair of antennas.[18] In other words, if $\mathbf{x}_i$ and $\mathbf{x}_j$ are two arbitrary, planar position vectors for the antennas in the array, then the *uv* point between them is simply

$$[u_{ij}, v_{ij}]^T = \mathbf{x}_i - \mathbf{x}_j \tag{3}$$

Although Eq. (3) results in the *uv* points having units of distance, it is common practice to normalize Eq. (3) by the wavelength of the incoming signal for aperture synthesis analysis. The calculation of the *uv* points for each combinatorial pair of antennas will generate a sampling pattern for the array; if the entire interferometer array is rotating (e.g., ground-based arrays follows Earth's rotation), then numerical propagation of the *uv* sampling pattern for a certain amount of time will generate the *uv* sampling track. The performance of the resultant interferometer array may, then, be characterized by numerous figures of merit, such as the full width at half maximum (FWHM) of the main beam and the smoothness of the resultant *uv* sampling pattern;[19] for an initial SMP bus deployment analysis, we focus on the latter.

The smoothness of the *uv* sampling pattern may be quantified by analyzing the resultant kernel density function. More specifically, we determine a high order polynomial fit to the UV sampling pattern kernel density function, and subsequently calculate the variance of the former with respect to the latter.[19] A lower variance of the polynomial fit, or polyfit, is indicative of a smoother *uv* plane coverage, and hence a preferable antenna geometry. Our current analysis consists of four primary antenna geometries: straight arm, spiral arm, concentrated spiral (in which more antennas are located at the center of a given spiral), and equidistant spiral (in which antennas are located at equidistant points along a given spiral). The concentrated and equidistant spiral geometries were calculated using the appropriate Archimedian spiral approximations. For each of the antenna geometries, the variance of a 3rd-order polyfit is computed for several configurations comprising of varying number of arms/spiral turns and antennas. The results of these simulations are provided in Figure 4 for each of the respective antenna geometries.

For the simulated antenna geometries, we note that the inclusion of curvature generally reduced the polyfit variance and may lead to smoother *uv* plane coverage. This can be specifically observed in the comparison of results for the straight arm and spiral arm geometries, where the variance of the polynomial fit decreases. Another notable observation for all simulated antenna geometries is that there might exist a saturation point, where increasing the number of antennas in the geometry adversely affects the interferometer performance. As such, caution must be exercised when selecting a configuration for a given antenna geometry. From the results in Figure 4, we note that variance of the kernel density polyfit of the equidistant spiral antenna geometry is of lower magnitude as compared to the other antenna geometries. Of the configurations modeled, the straight arm geometry has a maximum variance of $6.5 \times 10^3 \text{km}^2$, and the spiral arm geometry has a maximum variance of $5.3 \times 10^3 \text{km}^2$. In comparison, the equidistant spiral geometry has a maximum variance that is less than $3.5 \times 10^3 \text{km}^2$. Based on this observation, along with other trades, the equidistant spiral geometry is the current baseline configuration for the deployed SMP bus. The currently proposed concept assumes a 3 km diameter, 3-turn spiral comprised of 150 facelets, with one dipole antenna on each facelet. Despite an antenna geometry and equidistant antenna placement with a higher number of turns and larger diameters would provide better *uv* plane performance, a 3-turn spiral configuration is currently proposed after consideration of other design trades, including the size constraints on the
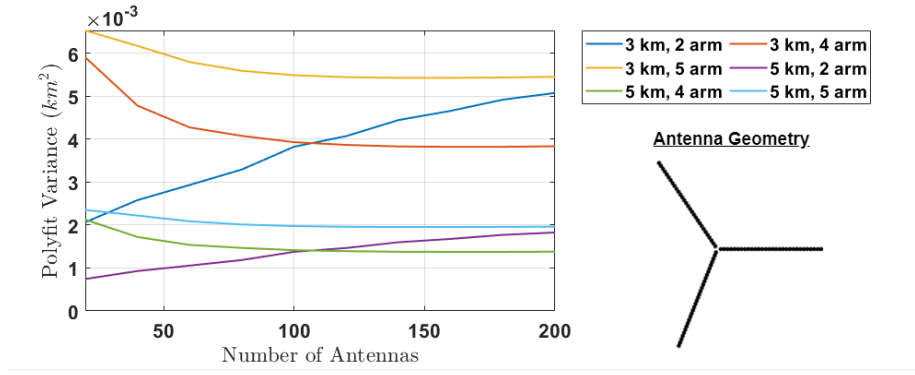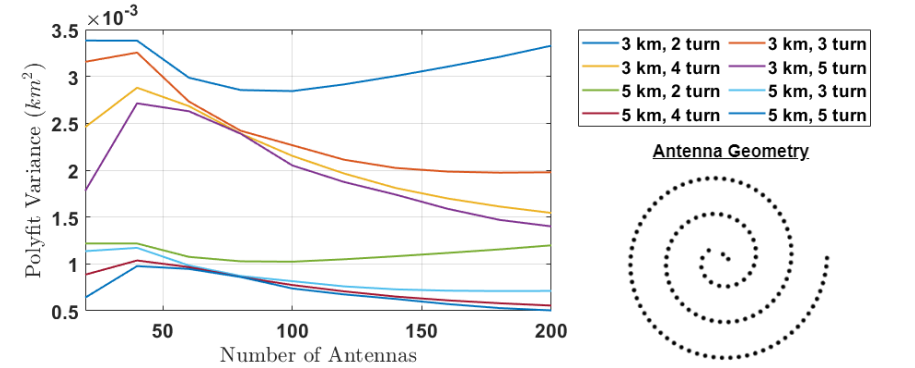
(a) Straight arm antenna geometry
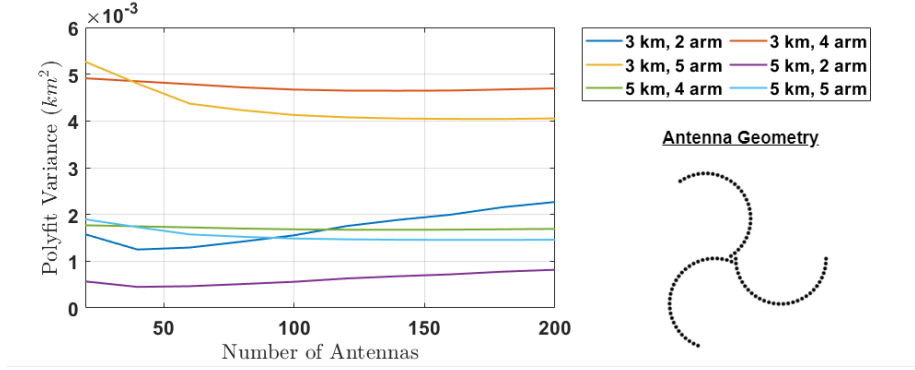
(b) Spiral arm antenna geometry
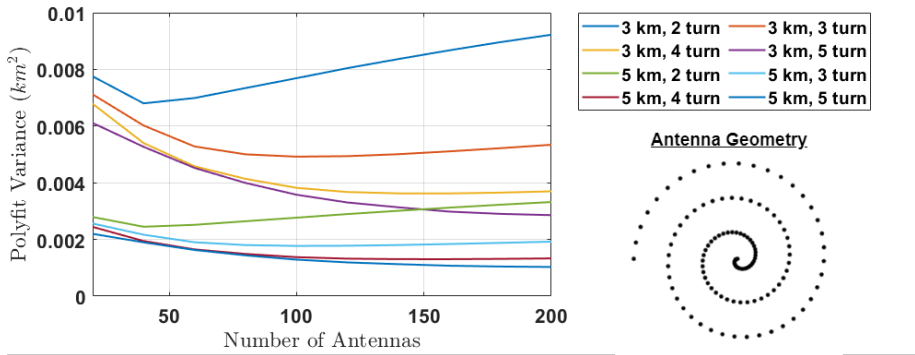
(c) Concentrated spiral antenna geometry.

(d) Equidistant spiral antenna geometry.

Figure 4: Simulated results for UV plane smoothness analysis, with various configurations in each subfigure denoting the diameter and the number of arms/turns of the geometry.
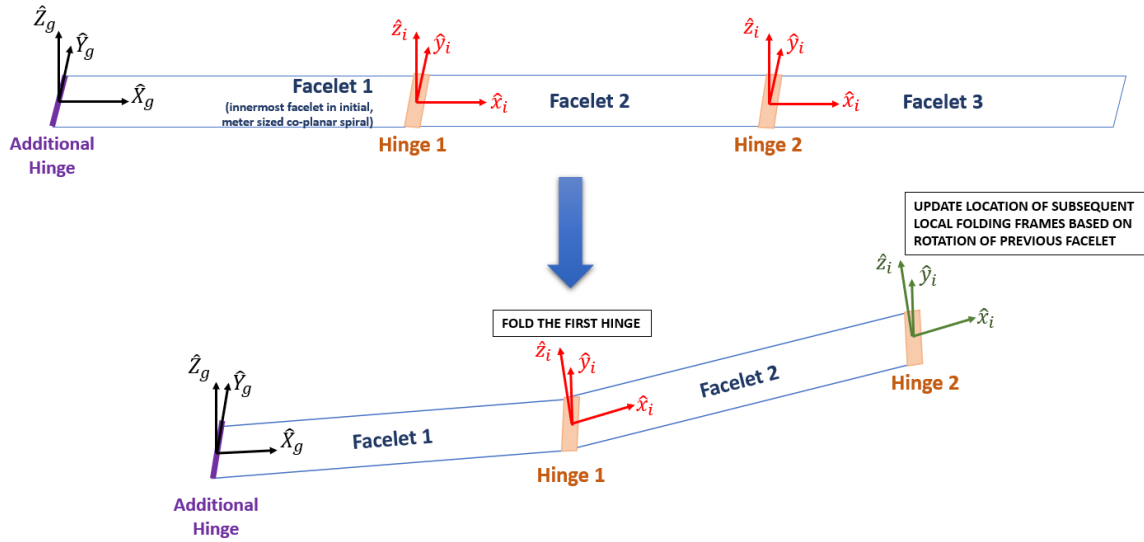
Figure 5: Modeling the spiral folding kinematics

spooled configuration imposed by the dimension of the payload fairing. Our chosen spiral configuration will require the SMP strip to have a length of roughly 15 kilometers, with each facelet being approximately 95 meters long.

DEPLOYMENT KINEMATICS

Folding angle variations at each ink hinge between a pair of adjacent facelets ultimately control how the SMP bus deploys from the rolled configuration into the final spiral geometry. The kinematics of such a deployment is discussed in the following section.

Kinematic Formulation

Consider a segment of the full SMP material, comprised of 3 facelets and 2 hinges, as illustrated in Figure 5. Multiple local floating frames $(\hat{x}_i, \hat{y}_i, \hat{z}_i)$ are fixed in each facelet (red coordinate systems in Figure 5). For each local floating $(\hat{x}_i, \hat{y}_i, \hat{z}_i)$, the origin is located at the center point of the *ith* hinge, the x_i axis aligned with the longer side of the facelet, the z_i axis orthogonal to the *ith* facelet, and the z_i axis completing a right-handed coordinate system. The hinge direction is described by a vector $\hat{h}_i$. Deployment kinematics may be rendered by assigning the orientation of the local floating frames at each epoch relative to an inertial, global frame $(\hat{X}_g, \hat{Y}_g, \hat{Z}_g)$, which is displayed in black in Figure 5. In our formulation, the inertial frame $(\hat{X}_g, \hat{Y}_g, \hat{Z}_g)$ is defined along an additional, "ghost" hinge imposed along the free edge of the first, or innermost, facelet of the initial, meter-sized co-planar, stored spiral.

The mathematical framework for the folding process is driven by basic kinematic relations. The local free floating frame $(\hat{x}_i, \hat{y}_i, \hat{z}_i)$ at each hinge may be rotated by an angle α_i relative to the preceding floating frame $(\hat{x}_{i-1}, \hat{y}_{i-1}, \hat{z}_{i-1})$ about the hinge direction, $\hat{h}_i$. The local facelet folding behavior is, essentially, rendered by an axis-angle representation $(\hat{h}_i, \alpha_i)$, from which the local rotation matrix $R_{i,local}$ for facelet *i* can be derived using the Rodrigues formula

$$R_{i,local} = I + \sin\alpha_i K + (1 - \cos\alpha_i)K^2 \tag{4}$$

8

Algorithm 1 Folding Kinematics

---

1. Define the location of the inertial frame, and its corresponding rotation matrix $R_{1,global}$, as computed from the axis-angle representation of the first, virtual hinge.

2. Define N, the total number of hinges

3. For hinge $i = 2$: N

    (a) Compute the current orientation of the ith local free floating frame: $[\hat{x}_i, \hat{y}_i, \hat{z}_i]^T_{update} = R_{i-1,global} \times [\hat{x}_i, \hat{y}_i, \hat{z}_i]^T$ and hinge axis $\hat{h}_{i,update} = R_{i-1,global}\hat{h}_i$

    (b) Compute the local rotation matrix R_i using the Rodrigues Formula and the updated axis-angle representation $\left(\hat{h}_{i,update}, \alpha_i\right)$

    (c) Compute the rotation matrix relative to the inertial frame: $R_{i,global} = R_i \times R_{i-1,global}$

---

where K is the skew symmetric matrix of the axis of rotation and I is a 3x3 identity matrix. Given a series of rotation angles, α_i, the geometry of the final Archimedian spiral is determined as follows. First, we assign the rigid rotation of the system relative to the inertial frame. As aforementioned, this is represented by the rotation of an additional local free floating frame that is included at the outermost edge of the innermost facelet in the initial, meter-sized coplanar spool. The corresponding axis-angle representation of this additional hinge is used to initialize the global rotation matrix $R_{1,global} = R_{1,local}$ for the first facelet. The global rotation matrix for each facelet, $R_{i,global}$, defines the orientation of the corresponding floating frame relative to the inertial frame. Then, for each subsequent facelet i, we first update the orientation of the free floating frame $(\hat{x}_i, \hat{y}_i, \hat{z}_i)$ relative to the inertial coordinate system by

$$[\hat{x}_i, \hat{y}_i, \hat{z}_i]^T_{update} = R_{i-1,global} \times [\hat{x}_i, \hat{y}_i, \hat{z}_i]^T \qquad (5)$$

Equation (5) updates the orientation of the next facelet's local free floating frame based on the rotation, relative to the inertial frame, induced by the folding of the previous facelet; this is visualized in Figure 5 by the green coordinate system. Note that we only update the orientation of this local frame relative to the global frame, and we do not change the relative rotation angle, α_i, between two adjacent facelets. Together with a rotation of the local free floating frame, we reorient the hinge axis relative to the global frame, $\hat{h}_{i,update} = R_{i-1,global}\hat{h}_i$. Using the now updated axis-angle representation $\left(\hat{h}_{i,update}, \alpha_i\right)$, we compute the local rotation matrix for the next facelet, R_i, relative to the previous, using the Rodrigues formula. Then, we compute the rotation matrix of the i-th facelet relative to the inertial frame using the rule for successive rotations

$$R_{i,global} = R_{i,local} \times R_{i-1,global} \qquad (6)$$

The current rotation matrix $R_{i,global}$ will then be used to update the location of the subsequent free floating frame, and the process will repeat until the last facelet. This numerical algorithm is summarized in Algorithm 1.

Derived Spiral Folding Methods

Using the kinematic relationships described in Algorithm 1, numerical simulation of various spiral deployment strategies is possible. Primarily, two main deployment strategies are considered: flat to spiral, and spiral to spiral. The flat to spiral strategy assumes that the initial configuration of

9

Table 1: Qualitative summary of considered SMP bus deployment strategies for kinematic analysis

	Flat to Spiral Approach	**Spiral to Spiral Approach**	
		Sequential	**Simultaneous**
Assumed initial configuration	SMP is already in a flat strip	SMP is wrapped in a meter-sized diameter co-planar spiral	
Base folding law	$f_{\text{spiral}} = \theta_{i,\text{fold Archimedian}}$ for hinge i = 1,2,...n	$f_{\text{spiral}} = (\theta_{i,\text{unfold}} + \theta_{i,\text{refold}})_{\text{Archimedian}}$ for hinge i = 1,2,...n	
Notable observations	Perfect desired final geometry achieved	Perfect desired final geometry achieved	Induced cornu spiral behavior, resulting in folding errors. This will require a corrective factor in base folding law, making it non-trivial to determine.
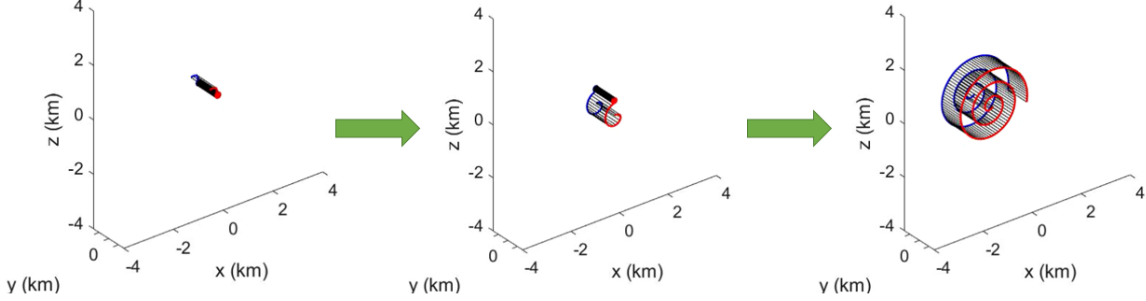
Figure 6: Visualization of the sequential spiral to spiral deployment strategy to achieve a desired geometry of a 3 km diameter, 3 turn spiral comprised of 150 facelets.

the SMP strip is flat; next, the SMP strip folds into the desired spiral geometry. The spiral to spiral method assumes an initial configuration of a meter-sized coplanar spool (such as one small enough to fit into the payload fairing of a launch vehicle); during deployment, the SMP strip simultaneously unfolds from the spool and refolds into the desired spiral geometry. The spiral to spiral method may be further divided into two variants: sequential hinge activation (where folding on only one hinge is activated at a time, in a sequential manner) and simultaneous hinge activation (where folding on all hinges is activated concurrently). Additionally a control logic gate that ensures no facelets intersect (i.e. fold into each other during deployment) was imposed within the simulation. A qualitative summary of the selected deployment strategies is given in Table 1, where the angle for the base folding law at each hinge is calculated using an Archimedian spiral basis.

From kinematic simulations, it was observed that we may achieve a perfect desired final spiral geometry using the flat to spiral and sequential spiral to spiral methods, whereas the simultaneous method results in an induced Cornu-spiral geometry of the deployed SMP bus. Furthermore, these folding errors persist despite changes in configuration, such as the diameter, number of turns, and the number of facelets. The spiral to spiral methods can fundamentally be classified as Cornu-spiral geometries; however, in sequential deployment we essentially unwrap one end of the Cornu-spiral and build the opposite end, whereas in the simultaneous deployment each of the ends of the Cornu-spiral behave in a manner that makes coordination and control of the folding process difficult and non-trivial. Engineering a feasible deployment sequence for the the simultaneous spiral to spiral strategy is non-trivial and requires more stringent analyses, as it will require the coordination of the simultaneous temporal folding variations; this additional complexity was not further investigated any may be the subject of future investigations. Consequently, the sequential spiral to spiral folding method is currently selected as the preferred baseline strategy from a kinematic standpoint. A visualization of the SMP deployment from roll to spiral is offered in Figure 6.

Folding Errors and Resultant Interferometer Performance

The sequential spiral to spiral method potentially enables to deploy the SMP bus into a perfect target geometry, under the assumption that exact folding angles are achieved at each ink hinge during unfolding. However, folding errors at each ink hinge are expected during deployment. Folding errors will likely result in a variation in the final antenna array geometry, and consequently affect the interferometeric performance. To further study this relation, the kinematic folding simulator and the UV plane performance simulator may be combined into a single framework. Next, the equidistant spiral antenna array geometry is considered due to its comparatively good interferometeric performance, as discussed previously.

There are two possible folding error scenarios during deployment: each hinge is perturbed by the same amount, and each hinge is perturbed by a random amount. The former was numerically modeled via perturbation of each hinge by the same amount randomly chosen from the range $\pm 5°$. Results for this consistently perturbed analysis are illustrated in Figure 7. It should be noted that the maximum baseline figure of merit is the largest distance between all combinatorial pairs of antennas, and is an important quantity in interferometery. The maximum baseline D relates the achieved angular resolution $\theta_{angular}$ and the signal wavelength λ via

$$\theta_{angular} = \frac{\lambda}{D} \tag{7}$$

Therefore, having a larger maximum baseline D will result in a better angular resolution, and consequently a more refined measurement of the incoming signal.

From Figure 7, it is observed that underfolding (i.e. negative angle perturbation) leads to the final deployed geometry resembling a Cornu spiral characterized by a large lateral distance in one of the planar directions. This geometry may result in larger maximum baselines and lower polyfit variance (which indicates better *uv* plane performance). While underfolding improves performance on the selected figures of merit, the impact of underfolding on the total moment of inertia of the deployed structure should be considered. Underfolding may cause the moment of inertia of the final structure to increase significantly over the baseline design value, potentially amplifying the effect of external perturbations while diminishing the authority of the attitude control system. In contrast to underfolding, the overfolding scenario leads to a more compact final spiral geometry, and an increasingly worse *uv* plane performance.

From a practical standpoint, it may be unlikely that the folding behavior at each hinge is perturbed by the same amount; rather, it is more likely that each hinge will be perturbed by different amounts. The residual effects of this scenario on the resultant *uv* plane performance were investigated via a Monte Carlo analysis. For each Monte Carlo trial, every hinge was perturbed by some random amount chosen from the range $\pm 5°$, with the spiral folding again being modeled via the sequential folding method. Simulation results for 2000 Monte Carlo trials are presented in Figure 8, with the average angle perturbation metric representing the average perturbation imposed on all hinges modeled. We again observe similar trends as those noted from Figure 7. A generally underfolded scenario leads to a Cornu spiral geometry, resulting in larger maximum baselines and lower polyfit variance, the latter indicating better *uv* plane performance. Though this may be desired from a scientific standpoint, having a larger maximum baseline may lead to the amplification of external perturbations and reducing the control authority of the structure, as noted previously. In contrast, generally overfolding leads to a more compact spiral geometry, and higher polyfit variance.

In both of the above analyses, we noted that overfolding leads to more compact spiral geometries and increasingly worse *uv* plane performance. From a practical standpoint, the prospect of overfold-

(a) Variation in maximum baseline

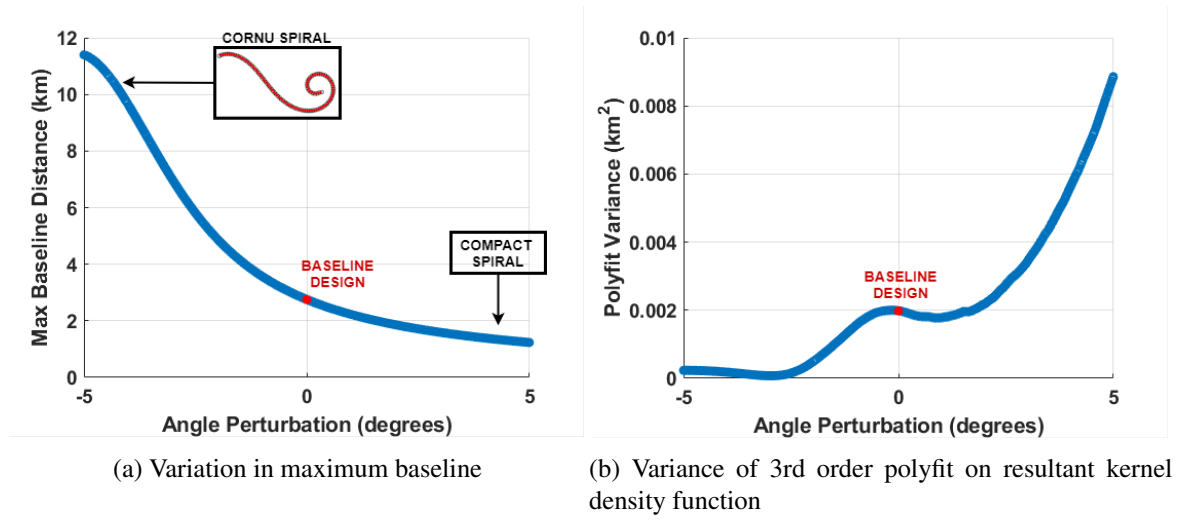(b) Variance of 3rd order polyfit on resultant kernel density function

Figure 7: Simulated results for constant amount perturbations in kinematic folding and resultant interferometer performance (red dot denotes the current baseline design).
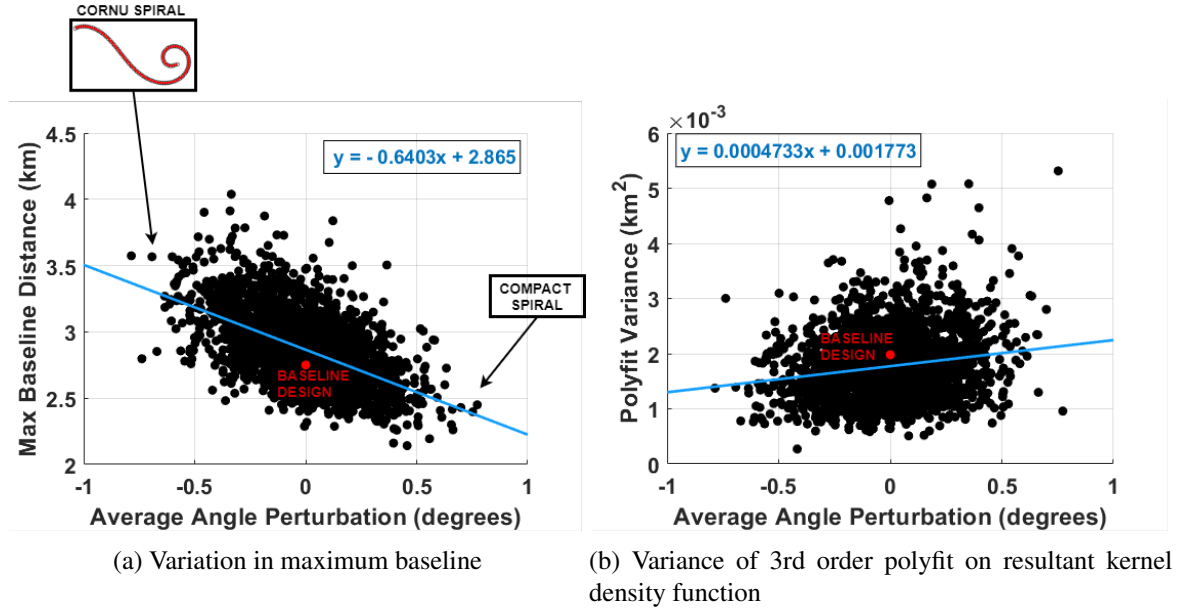

(a) Variation in maximum baseline

(b) Variance of 3rd order polyfit on resultant kernel density function

Figure 8: Numerical results for Monte Carlo simulations in kinematic folding, where each hinge is randomly perturbed by some amount in the range $\pm 5°$ and resultant interferometer performance (red dot denotes the current baseline design).

ing the hinges can be mitigated by the inclusion of a self-concealing mechanism, one that blocks the ink hinge from any additional IR absorption. Mechanical methods (e.g., mechanical interference and spring mechanisms), chemical methods (e.g., self-evaporating ink), as well as dynamical methods (e.g., hinge self-shadowing due the a change of geometry during folding) may be viable options.
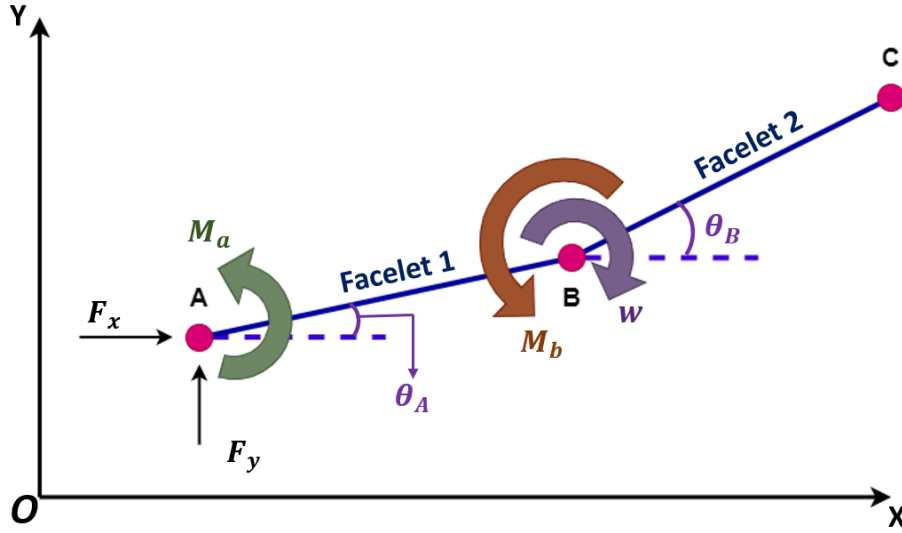
Figure 9: Free body diagram for reduced fidelity dynamical modeling

DEPLOYMENT DYNAMICS

In conjunction with the deployment kinematics, we have also started analyzing the deployment dynamics for the unfolding of the SMP-based antenna array from the rolled to the operative configuration. Currently, we focused on reduced fidelity modeling of the planar dynamics for an elementary SMP unit which comprises two facelets and one hinge. It was also assumed that each facelet has uniform mass distribution.

Derivation of Equations of Motion for an Elementary SMP Unit

The reduced fidelity dynamical model of the SMP facelet-hinge-facelet elementary system is, in essence, a modified, planar double pendulum with free end points and damping on the central hinge; this model is illustrated in Figure 9. The SMP facelet-hinge-facelet elementary system is modeled with 4 degrees of freedom: x, y, θ_A, θ_B. With reference to Figure 9, the selected degrees of freedom define the position of points of the first free end point, A, the hinge point B, and the second free end point, C, as

$$\vec{r}_{AO} = [x, y]^T, \quad \vec{r}_{BA} = [l_1 \cos\theta_A, l_1 \sin\theta_A]^T, \quad \vec{r}_{CB} = [l_2 \cos\theta_B, l_2 \sin\theta_B]^T \tag{8}$$

where l_1 and l_2 are the lengths of each facelet, and O is the origin of the inertial frame. These 4 degrees of freedom are sufficient to describe the planar motion of the elementary facelet-hinge-facelet system.

The resultant dynamical behavior of the modeled system is driven by two external, nonconservative forces and two internal nonconservative force. An external force $\bar{F} = [F_x, F_y, 0]^T$ may be exerted at point A, and may induce a rigid translational, relative to O, of the entire system. An external moment $\bar{M}_A = [0, 0, M_A]^T$ may be exerted at point A, and may induce a rigid rotation of the entire system. The internal hinge torque M_b and hinge damping factor w are included to mimic the folding behavior of facelet 2 relative to facelet 1. In terms of the four degrees of freedom, the

nonconservative work due to both internal and external forces can be written in variational form as

$$\delta \bar{W}_{nc} = (F_x l_1 \cos \theta_A + F_y l_1 \sin \theta_A + M_a + T_{1,internal})\delta \theta_A$$
$$+(F_x l_2 \cos \theta_B + F_y l_2 \sin \theta_B + T_{2,internal})\delta \theta_B \qquad (9)$$
$$+F_x x \delta x + F_y y \delta y$$

where $T_{1,internal}$ and $T_{2,internal}$ are the resultant internal torque on facelets 1 and 2 due to the internal torque M_b and damping w , and are defined as

$$T_{1,internal} = -M_b + w(\dot{\theta}_B - \dot{\theta}_A)$$
$$T_{2,internal} = M_b - w(\dot{\theta}_B - \dot{\theta}_A) \qquad (10)$$

As a first approximation, the system is assumed to be a "free floater", therefore, gravity is not included in our dynamical model (i.e., $g = 0$). The full equations of motion (EOM) for the elementary SMP unit are derived using Lagrangian mechanics; by defining the four degrees of freedom as the generalized coordinated q_k, where $k = 1...4$, the second order differential equations of motion for each degree of freedom can be derived in the Lagrange equation form

$$\frac{d}{dt}\left(\frac{\partial T}{\partial \dot{q}_k}\right) - \frac{\partial T}{\partial q_k} = Q_k \qquad (11)$$

where Q_k are the generalized nonconservative forces, and are derived from Eq. 9. The kinetic, energy, T, for the elementary SMP unit is derived as

$$T = \frac{1}{2}m_1 \left(\dot{\theta}_A{}^2 \frac{l_1^2}{4} - \dot{x}\dot{\theta}_A l_1 \sin \theta_A + \dot{y}\dot{\theta}_A l_1 \cos \theta_A + \dot{x}^2 + \dot{y}^2\right)$$
$$+\frac{1}{2}m_2 \left(\dot{\theta}_A{}^2 l_1^2 + \dot{\theta}_B{}^2 \frac{l_2^2}{4} - \dot{\theta}_B \dot{x} l_2 \sin \theta_B - 2\dot{\theta}_A l_2 \dot{x} \sin \theta_A + 2\dot{\theta}_A \dot{y} l_2 \cos \theta_A\right) + \qquad (12)$$
$$+\frac{1}{2}m_2 \left(\dot{\theta}_B \dot{y} l_2 \cos \theta_B + \dot{\theta}_A \dot{\theta}_B l_1 l_2 \cos (\theta_A - \theta_B) + \dot{x}^2 + \dot{y}^2\right) + \frac{1}{2}I_1 \dot{\theta}_A{}^2 + \frac{1}{2}I_2 \dot{\theta}_B{}^2$$

Using Eq. 9, 11 and 12, the full EOM for the elementary SMP system illustrated in Figure 9 are derived to be

$$\ddot{x}(m_1 + m_2) = Q_1 + \frac{m_1 l_1}{2}\left(\ddot{\theta}_A \sin \theta_A + \dot{\theta}_A \dot{\theta}_A \cos \theta_A\right) + \frac{m_2 l_2}{2}\left(\ddot{\theta}_B \sin \theta_B + \dot{\theta}_B \dot{\theta}_B \cos \theta_B\right)$$
$$+m_2 l_2 \left(\ddot{\theta}_A \sin \theta_A + \dot{\theta}_A \dot{\theta}_A \cos \theta_A\right) \qquad (13)$$

$$\ddot{y}(m_1 + m_2) = Q_2 - \frac{m_1 l_1}{2}\left(\ddot{\theta}_A \cos \theta_A - \dot{\theta}_A \dot{\theta}_A \sin \theta_A\right) - m_2 l_2 \left(\ddot{\theta}_A \cos \theta_A - \dot{\theta}_A \dot{\theta}_A \sin \theta_A\right)$$
$$-\frac{m_2 l_2}{2}\left(\ddot{\theta}_B \cos \theta_B - \dot{\theta}_B \dot{\theta}_B \sin \theta_B\right) \qquad (14)$$

14

$$\ddot{\theta}_A \left(I_1 + \frac{m_1}{2}l_1^2 + m_2 l_1^2 \right) = Q_3 + \frac{m_1}{2} \left(\ddot{x} \sin\theta_A + \dot{x}\dot{\theta}_A \cos\theta_A \right) - \frac{m_1}{2} \left(\ddot{y} \cos\theta_A - \dot{y}\dot{\theta}_A \sin\theta_A \right)$$
$$+ \frac{m_2}{2} \left(\ddot{x} \sin\theta_A + \dot{x}\dot{\theta}_A \cos\theta_A \right) - m_1 l_2 \left(\ddot{y} \cos\theta_A - \dot{y}\dot{\theta}_A \sin\theta_A \right)$$
$$- \frac{m_2 l_1 l_2}{2} \left(\ddot{\theta}_B \cos(\theta_A - \theta_B) - \dot{\theta}_B(\dot{\theta}_A - \dot{\theta}_B) \sin(\theta_A - \theta_B) \right)$$
$$- \frac{m_1}{2} \left(\dot{x}\dot{\theta}_A l_1 \cos\theta_A + \dot{y}\dot{\theta}_A l_1 \sin\theta_A \right)$$
$$- \frac{m_2}{2} \left(2\dot{\theta}_A l_2 \dot{x} \cos\theta_A + 2\dot{\theta}_A \dot{y} l_2 \sin\theta_A + \dot{\theta}_A \dot{\theta}_B l_1 l_2 \sin(\theta_A - \theta_B) \right)$$
$$\text{(15)}$$

$$\ddot{\theta}_B \left(I_2 + \frac{m_2 l_2^2}{2} \right) = Q_4 + \frac{m_2 l_2}{2} \left(\ddot{x} \sin\theta_B + \dot{x}\dot{\theta}_B \cos\theta_B \right) - \frac{m_2 l_2}{2} \left(\ddot{y} \cos\theta_B - \dot{y}\dot{\theta}_B \sin\theta_B \right)$$
$$- \frac{m_2 l_1 l_2}{2} \left(\ddot{\theta}_A \cos(\theta_A - \theta_B) - \dot{\theta}_A(\dot{\theta}_A - \dot{\theta}_B) \sin(\theta_A - \theta_B) \right)$$
$$+ \frac{m_2}{2} \left(\dot{\theta}_A \dot{\theta}_B l_1 l_2 \sin(\theta_A - \theta_B) - \dot{\theta}_B \dot{x} l_2 \cos\theta_B - \dot{\theta}_B \dot{y} l_2 \sin\theta_B \right)$$
$$\text{(16)}$$

Additionally, each of the second order differential EOM may be normalized with respect to the proper base units (i.e T, L, M) for each of the degrees of freedom. The EOM for $\ddot{x}$ and $\ddot{y}$ may be normalized by the factor $\frac{T^2}{L}$, and the EOM for $\ddot{\theta}_A$ and $\ddot{\theta}_B$ may be normalized by the factor T^2. The normalization of these EOM allows for preliminary sensitivity analyses for the underlying nondimensional ratios. From a nondimensionalization analysis (omitted for brevity), inertia loading of the deployed SMP bus appears as one of the most critical factors for deployment of the SMP-based antenna array, as it essentially counteracts the folding behavior induced by the hinge torque M_b and potentially yield structural collapse (i.e. uncontrolled deformation that induced undesired folding behavior).

Preliminary Deployment Feasibility Analysis

The derivation of the respective EOM for each degree of freedom allowed for various dynamical simulations. The possibility of structural collapse driven by inertia loads during the SMP bus deployement is a critical determinant for the feasibility of the proposed mission concept. For a first analysis, we define feasibility as folding of the simplified SMP system reflecting in the desired direction (i.e. θ_B increases and $\theta_B > \theta_A$) as it results from propagating the equations of motion in Eq. (11). By defining the folding angle θ_{fold} as $\theta_{fold} = \theta_B - \theta_A$ we can preliminary evaluate both the feasibility, as well as the time needed to fold the SMP by a desired amount.

Using the derived dynamical EOM, we can simulate the feasibility of folding during the full deployment process. By proceeding in a sequential manner, as each facelet i is deployed, recalculate the SMP bus mass as $m_{i,2} = m_{facelet} \times i$, and the mass of the remaining SMP material in the initial, meter-sized co-planar spool as $m_{i,1} = m_{total} - m_{i,2}$ ($m_{facelet}$ is the mass of each facelet, and is assumed to be the same for all facelets, and m_{total} is the total mass of the full SMP strip). Based on these mass values, we then appropriately calculate the respective inertias of the deployed SMP bus and the remaining SMP material still spooled in the initial configuration. The inertias are computed from the assumption of a rigid disk geometry, whose radii are appropriately referenced from the corresponding Archimedian spiral approximation (as the deployment progresses, the radius of the SMP bus will increase, whereas the radius of the SMP material remaining in the initial, co-planar
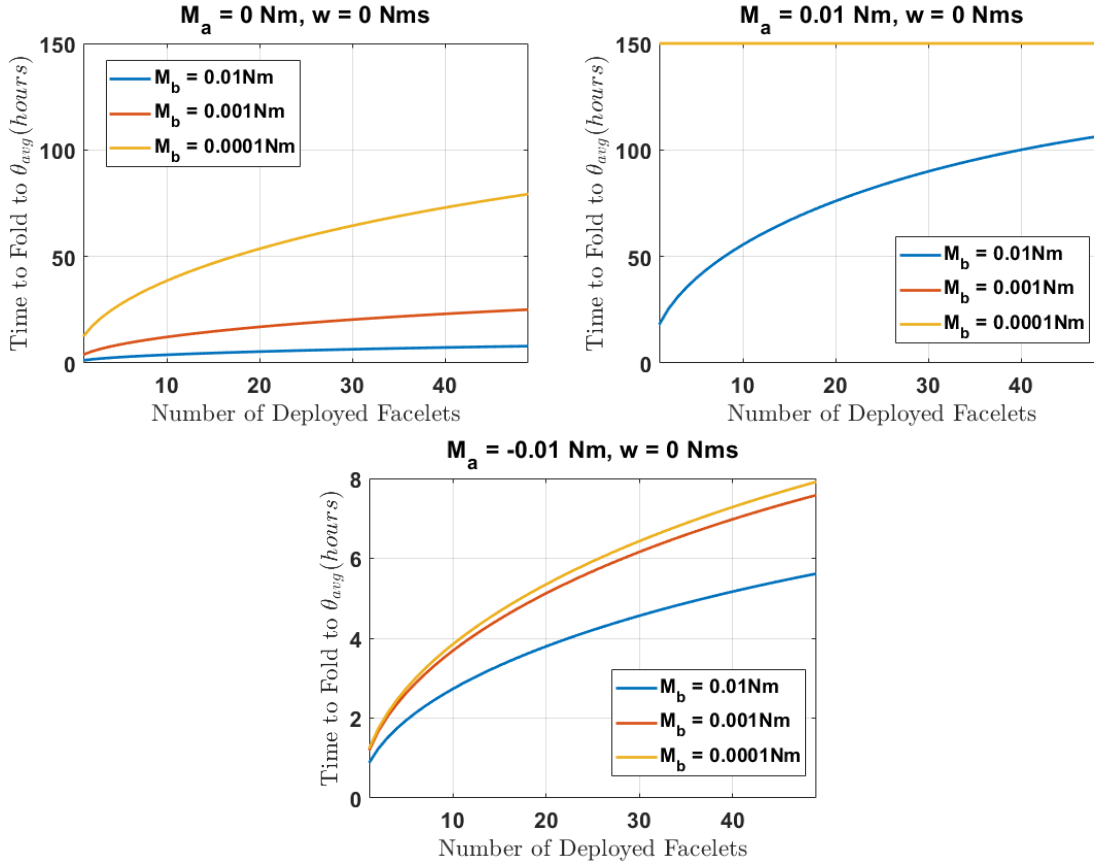
15

Figure 10: Folding times to reach $\theta_{avg} \approx 64°$ as deployment progresses

spool configuration will decrease). This process is repeated as each facelet is deployed, with numerical simulation proceeding until either the desired θ_{fold} is achieved, or the maximum folding epoch allowed is exceeded.

Along with the feasibility, the effect of various spin torques M_a, hinge torque M_b and hinge damping factor w on the resultant folding behavior may be analyzed. For our baseline design, using the previously discussed sequential spiral folding method to deploy the SMP strip from an initial, meter sized diameter to our current final baseline configuration (3 km diameter, 3 turn spiral with 150 facelets), the average required folding angle is $\theta_{avg} \approx 64°$. Furthermore, consider three spin torque scenarios: no spin ($M_a = 0$), constant prograde spin torque (scalar $M_a > 0$), and constant retrograde spin torque (scalar $M_a < 0$). Numerical results for required folding time to achieve $\theta_{avg} \approx 64°$ are provided in Figure 10 with nonzero spin torque magnitude $|M_a| = 0.01$ Nm, no damping factor ($w = 0$ Nms), and various hinge torques. Furthermore, there are no translational forces imposed (i.e. $F_x = F_y = 0$), and the mass of each facelet is assumed to be $m_{facelet} = 30$ kg. while these results are for a specific scenario, the noted observations are consistent for other values of M_a and w; it should be noted that the inclusion of damping at the hinge will generally increase the folding time required to achieve θ_{avg}, as it opposes the folding behavior induced by the hinge torque.

For a no spin torque scenario, we observe that as deployment progresses, the required folding time to achieve θ_{avg} increases, with lower hinge torques requiring higher folding times as they need

16

to overcome increasing inertia loading from the deployed SMP bus. For a constant prograde spin torque scenario, there is no feasibility of folding to achieve θ_{avg} for M_b magnitudes $\leq 10^{-3}$ Nm; a maximum folding time of 150 hours was imposed on the numerical integration scheme, and this was reached before any of the facelets had folded to θ_{avg}. Based on this result, as well as other scenarios which yielded the same observations, a prograde spin torque scenario may result in an unfeasible deployment strategy as the hinge torque is unable to overcome the induced inertia loading. Conversely, the constant retrograde spin scenario results yielded a viable path to deployment. We observe that as deployment progresses, the folding time also increases, similar to the no spin scenario; however, the magnitude of folding time required is significantly lower, resulting in a potentially feasible deployment scenario.

PROPOSED DEPLOYMENT STRATEGY

Kinematic and dynamical analysis may inform the deployment strategy for the proposed SMP-based antenna array. From kinematic simulations, a sequential folding strategy appears as the most promising among the three analyzed. Sequential folding not only allows for deployment from an initial, meter sized spiral to a final configuration that has a kilometer sized diameter, but also results into a perfect nominal geometry assuming no folding errors occur. From dynamical simulations, we observed that inertial loads due to centripetal or angular acceleration may quickly overcome the predicted hinge torque that would be induced by the polymer relaxation at the hinge region. To enable SMP-based antenna array deployment within scenario that are dominated by inertial loads, the folding direction should align the direction of application of the inertial loads. For example,maintaining a constant spin torque M_a in the direction opposite to the final spiral folding may aid the deployment process. Higher M_a values result in lower folding times, but there may exist a maximum limit in terms of maximum torque value, M_a, that can be produced from mechanical actuation devices.

Leveraging insight gathered from kinematic and dynamical analysis, a possible deployment strategy for the SMP-based antenna array is illustrated in Figure 11. The initial, meter sized spool may be housed within a central hub, that shields the SMP material from the space environment until the deployment process is initiated. During deployment, a constant spin torque is applied to the central hub. The spin torque is applied in the direction opposite to the folding of final spiral geometry. If a low lunar orbit with solar umbra and penumbra regions is employed as a orbit baseline, the deployment process may occur progressively during the periods in sun-light. Upon achieving the final spiral geometry, the spin torque at the central hub is removed and deployed structure may maintain a constant spin rate for passive attitude stabilization. However, the utilization of spin stabilization has not been fully analyzed yet, and warrants further investigation.

CONCLUDING REMARKS

The creation and evolution of the Universe may be divided into distinct phases, the majority of which have been characterized by observational evidence. However, the Dark Ages period remains a scientific puzzle, as the corresponding redshifted 21-cm signal is at low and very-low radio frequencies($\leq$ 30 MHz). At these low and very low frequencies ground-based 21-cm signal observations are rendered basically infeasible by the Earth's ionosphere as well as man-made radio interference. The natural solution may be to move the 21-cm signal observatory to space, outside the reach of both natural and artificial interferences. A self-folding SMP bus with embedded radio frequency receivers may enable to develop a largescale, space-borne antenna array capable of cap-
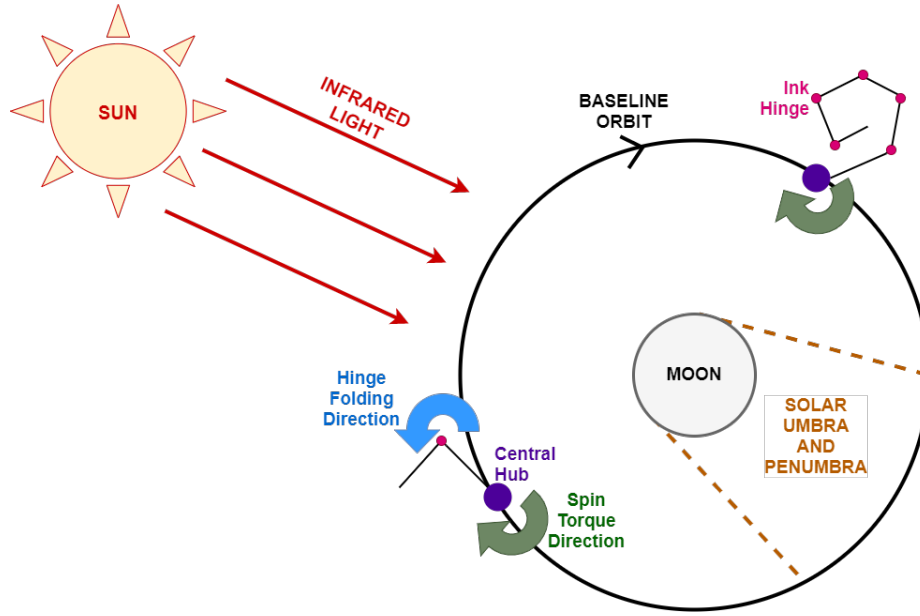
Figure 11: Visualization of the proposed deployment strategy.

turing signals in the frequency band nearby 30 MHz. The SMP bus is patterned with ink hinges that induce a predetermined deformation of the SMP strip when exposed to solar energy. As a consequence of this deformation, the SMP bus may self-deploy from a stored configuration to a large spiral. This process results in a connected system of several receivers that can act as an orbiting antenna array for very-low frequency astronomy.

In this work we initiated the process of designing and analyzing the appropriate strategy to deploy our SMP material from a meter-sized diameter co-planar spool into a kilometer-sized final configuration. This process was initialized by preliminary considerations on the scientific return of our antenna array, as quantified by the resultant *uv* plane performance of the deployed SMP bus geometry. Analysis of various antenna geometries, each with multiple configurations, resulted in an equidistant antenna placement along a spiral to be an appropriate geometry for *uv* plane coverage. Now faced with the prospect of deploying the SMP bus into a spiral geometry, kinematic analyses concluded that a deployment method in which we only activate one hinge at a time, in a sequential manner, is a practical approach at achieving our desired geometry. Relations between hinge over/under folding are also analyzed via Monte Carlo trials, and it is observed that general underfolding of the SMP bus results in a elongated Cornu spiral final geometry, whereas general overfolding results in a more compact spiral. Finally, reduced fidelity dynamical simulations, whose corresponding equations of motion are derived from a modified double pendulum model, indicate that inducing a spin torque in the direction opposing the hinge folding behavior may significantly help the deployment process due to the induced inertia loading. These conclusions are then incorporated to derive a preliminary strategy to actively deploy a kilometer-sized SMP bus from an initial meter sized spooled configuration in order to construct an orbiting interferometer array to observe the global Dark Ages signal.

ACKNOWLEDGMENT

REFERENCES

[1] J. Miralda-Escudé, "The Dark Age of the Universe," *Science*, Vol. 300, June 2003.

[2] D. L. Jones, T. Joseph, W. Lazio, and J. O. Burns, "Dark Ages Radio Explorer Mission: Probing the Cosmic Dawn," *IEEE Aerospace Conference, Big Sky, Montana*, March 2015.

[3] J. Lazio, C. Carilli, J. Hewitt, S. Furlanetto, and J. Burns, "The lunar radio array (LRA)," *UV/Optical/IR Space Telescopes: Innovative Technologies and Concepts IV* (H. A. MacEwen and J. B. Breckinridge, eds.), Vol. 7436, International Society for Optics and Photonics, SPIE, 2009, pp. 177 – 187, 10.1117/12.827955.

[4] J. Burns, G. Hallinan, J. Lux, A. Romero-Wolf, T. Chang, J. Kocz, J. Bowman, R. Macdowall, J. Kasper, R. Bradley, M. Anderson, and D. Rapetti, "FARSIDE: A Low Radio Frequency Interferometric Array on the Lunar Farside," *Astro2020 APC White Papers*, 2020.

[5] A. Boonstra, N. Saks, H. Falcke, M. Wolt, M. Bentum, R. T. Rajan, M. Wijnholds, M. J. Arts, C. v. t. Klooster, and F. Belien, "DARIS : a low-frequency distributed aperture array for radio astronomy in space," 01 2010.

[6] L. Buinhas, K. Frankl, H. Linz, and R. Förstner, "IRASSI infrared space interferometer: Formation geometry and relative dynamics analysis," *Acta Astronautica*, Vol. 153, 2018, pp. 394 – 409.

[7] S. Wu, W. Chen, Y. Zhang, W. A. Baan, and T. An, "SULFRO: a Swarm of Nano-/Micro-Satellite at SE L2 for Space Ultra-Low Freqneucy Radio Observatory," *28th AIAA/USU Conference on Small Satellites, Logan, Utah*, 2014.

[8] M. Bentum, E. Gill, C. Verhoeven, A.-J. Veen, and A. Boonstra, "A novel astronomical application for formation flying small satellites," *60th International Astronautical Congress, Daejeon, Republic of Korea*, October 2009.

[9] R. T. Rajan, S. Engelen, M. Bentum, and C. Verhoeven, "Orbiting Low Frequency Array for radio astronomy," *IEEE Aerospace Conference*, 2011, pp. 1–11.

[10] R. R. Weber, J. K. Alexander, and R. G. Stone, "The radio astronomy explorer satellite, a low-frequency observatory," *Radio Science*, Vol. 6, No. 12, 1971, pp. 1085–1097, 10.1029/RS006i012p01085.

[11] J. Burns, T. Lazio, S. Bale, J. Bowman, R. Bradley, C. Carilli, S. Furlanetto, G. Harker, A. Loeb, and J. Pritchard, "Probing the First Stars and Black Holes in the Early Universe with the Dark Ages Radio Explorer (DARE)," *Advances in Space Research*, Vol. 49, June 2011, 10.1016/j.asr.2011.10.014.

[12] R. Mailen, M. Dickey, J. Genzer, and M. Zikry, "Effects of thermo-mechanical behavior and hinge geometry on folding response of shape memory polymer sheets," *Journal of Applied Physics*, Vol. 122, 11 2017, p. 195103, 10.1063/1.5000040.

[13] T. Liu, L. Liu, M. Yu, Q. Li, C. Zeng, X. Lan, Y. Liu, and L. Jinsong, "Integrative hinge based on shape memory polymer composites: Material, design, properties and application," *Composite Structures*, Vol. 206, 08 2018, 10.1016/j.compstruct.2018.08.041.

[14] M. Zarek, M. Layani, I. Cooperstein, E. Sachyani, D. Cohn, and S. Magdassi, "3D Printing: 3D Printing of Shape Memory Polymers for Flexible Electronic Devices (Adv. Mater. 22/2016)," *Advanced Materials*, Vol. 28, 06 2016, pp. 4166–4166, 10.1002/adma.201670148.

[15] R. Barkana, M. Bentum, G. Bernardi, A. Boonstra, J. Bowman, J. Burns, X. Chen, A. Datta, H. Falcke, A. Fialkov, B. K. Gehlot, L. Gurvits, V. Jelić, M. Wolt, L. Koopmans, J. Lazio, D. Meerburg, G. Mellema, and P. Zarka, "Peering into the Dark (Ages) with Low-Frequency Space Interferometers," August 2019.

[16] S. Jester and H. Falcke, "Science with a lunar low-frequency array: From the dark ages of the Universe to nearby exoplanets," *New Astronomy Reviews*, Vol. 53, May 2009, p. 1–26, 10.1016/j.newar.2009.02.001.

[17] K.-W. M. e. al., "Dark Ages Explorer-DEX, a white paper for a low frequency radio interferometer mission to explore the cosmological dark ages for the L2," *L3 ESA Cosmic Vision Program*, 2013.

[18] R. T. Rajan, A. Boonstra, M. Bentum, M. Wolt, F. Belien, M. J. Arts, N. Saks, and A.-J. Veen, "Space-based Aperture Array For Ultra-Long Wavelength Radio Astronomy," *Experimental Astronomy*, Vol. 41, 05 2015, pp. 271–306, 10.1007/s10686-015-9486-6.

[19] E. Keto, "Hierarchical configurations for cross-correlation interferometers with many elements," *Journal of Astronomical Instrumentation*, Vol. 1, No. 1, 2012.